

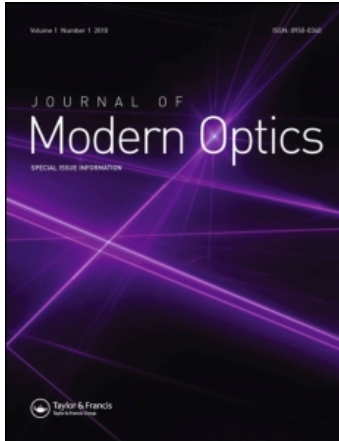
This article was downloaded by: [Friedrich Althoff Konsortium]

On: 23 March 2011

Access details: Access Details: [subscription number 907681674]

Publisher Taylor & Francis

Informa Ltd Registered in England and Wales Registered Number: 1072954 Registered office: Mortimer House, 37-41 Mortimer Street, London W1T 3JH, UK



## Journal of Modern Optics

Publication details, including instructions for authors and subscription information:

<http://www.informaworld.com/smpp/title~content=t713191304>

### Computational nano-optic technology based on discrete sources method

Elena Eremina<sup>a</sup>; Yuri Eremin<sup>b</sup>; Thomas Wriedt<sup>c</sup>

<sup>a</sup> University of Bremen, Bremen 28359, Germany <sup>b</sup> Moscow Lomonosov State University, Moscow 119991, Russia <sup>c</sup> Institut für Werkstofftechnik, Bremen 28359, Germany

First published on: 11 October 2010

**To cite this Article** Eremina, Elena , Eremin, Yuri and Wriedt, Thomas(2011) 'Computational nano-optic technology based on discrete sources method', Journal of Modern Optics, 58: 5, 384 – 399, First published on: 11 October 2010 (iFirst)

**To link to this Article:** DOI: 10.1080/09500340.2010.515751

**URL:** <http://dx.doi.org/10.1080/09500340.2010.515751>

PLEASE SCROLL DOWN FOR ARTICLE

Full terms and conditions of use: <http://www.informaworld.com/terms-and-conditions-of-access.pdf>

This article may be used for research, teaching and private study purposes. Any substantial or systematic reproduction, re-distribution, re-selling, loan or sub-licensing, systematic supply or distribution in any form to anyone is expressly forbidden.

The publisher does not give any warranty express or implied or make any representation that the contents will be complete or accurate or up to date. The accuracy of any instructions, formulae and drug doses should be independently verified with primary sources. The publisher shall not be liable for any loss, actions, claims, proceedings, demand or costs or damages whatsoever or howsoever caused arising directly or indirectly in connection with or arising out of the use of this material.

## Computational nano-optic technology based on discrete sources method

Elena Eremina<sup>a</sup>, Yuri Eremin<sup>b</sup> and Thomas Wriedt<sup>c\*</sup>

<sup>a</sup>University of Bremen, Badgasteiner Str. 3, Bremen 28359, Germany; <sup>b</sup>Moscow Lomonosov State University, Lenin's Hills, Moscow 119991, Russia; <sup>c</sup>Institut für Werkstofftechnik, Badgasteiner Str. 3, Bremen 28359, Germany

(Received 15 June 2010; final version received 3 August 2010)

Continuous advance in the potential of fabrication and utilization of nanostructures for different applications requires an adequate tool for such structures' analysis and characterization. Investigation of light scattered by nanostructures by means of computer simulation seems to be a reliable tool for investigation of the properties and functional abilities of nanostructures. In particular, nano-features embedded in layered structures are of growing interest for many practical applications. Mathematical modeling of light scattering allows us to predict functional properties and behavior of nanostructures prior to their fabrication. This helps to reduce manufacturing and experimental costs. In the present paper, the Discrete Sources Method (DSM) is used as a tool of computational nano-optics. Mathematical models based on DSM are used for several practical applications. We are going to demonstrate that the computer simulation analysis allows not only prediction and investigation of the system properties, but can help in development and design of new setups.

**Keywords:** nanostructure; light scattering; mathematical modeling; discrete sources method; extreme transmission effect; total internal reflection microscopy

### 1. Introduction

Nanoscience and nanotechnology are widely seen as having huge potential to bring benefits to many areas of human life. Nowadays nanotechnologies are already implemented in areas as diverse as pharmaceuticals development, water decontamination, information and communication technologies, production of computers, and materials with new interesting properties. With further development and miniaturization of nanostructures, there is a need for a detailed analysis of their structure and composition down to the molecular level. The analysis of light scattering by nanostructures is a convenient tool to investigate the structures' properties, such as size, shape, composition, imperfection, etc. Because of the difficulties, limitations, and high costs of nano-fabrication, it is of advantage when nanostructures are modeled and analyzed by means of computer simulation prior to their fabrication. To reduce production costs, it is highly important to perform an accurate and well-validated simulation analysis.

Compared with measuring techniques, mathematical modeling and computer simulation are inexpensive and flexible tools for investigation, analysis and prediction of the scattering behavior of nanostructures. Once realized, computer models can be easily adjusted

to different features of a designed structure or special schemes of an experimental setup. Employing the computer model allows prediction of fundamental scattering properties of an entire system, discovering of new effects, suggestion of new schemes for experimental setup and solving metrology problems. Additionally, modeling of the nanostructures' properties and analyzing their light scattering behavior can be used for a correct interpretation of measured data.

For three-dimensional light scattering simulation, accurate modeling requires an appropriate choice of method. Since the most interesting nanoeffects are based on resonances, the corresponding computer model must be based on rigorous Maxwell theory. There are multiple approaches, which have been applied to light scattering analysis: Finite Difference Time Domain (FDTD) [1], Finite Element Method (FEM) [2], Coupled Dipole Approximation (CDA) [3], Volume Integral Equation (VIE) [4], Multiple MultiPole Technique (MMP) [5], T-matrix method [6] and Discrete Sources Method (DSM) [7]. However, most of these methods have different characteristics, restrictions and advantages. The advantage of pure numerical methods, such as the FDTD or the FEM, is the ease of implementation. They are applied directly to Maxwell equations.

\*Corresponding author. Email: thw@iwt.uni-bremen.de

Because of this, there has been a strong trend towards FDTD solvers in the last few decades. FDTD is a simple technique, because it does not require profound knowledge of Maxwell theory. It is based on simple mathematical operations, which can be handled even by very simple computers. Time domain formulations have big advantages when non-linear materials are present, but they are not really well suited for dispersive materials with strong nonlinearities in their frequency response. To overcome problems caused by dispersion, various simplified media models (Debye, Drude, Lorentz, etc.) were incorporated in FDTD models. Unfortunately, these models are not accurate enough in many cases [8]. Furthermore, they cause difficulties in the implementation and problems with stability of the computer codes. Besides, they increase the required computer memory and computation time. Additionally, a conventional FDTD scheme does not account for infinite plane interfaces and does not use special tricks to approximate it [9].

The simplest way to get rid of problems connected with materials dispersion is to work in the frequency domain. This approach leads to direct methods, such as the FEM [2]. The FEM implementation leads to matrix equations with large sparse matrices. The approach allows one to reach a very high accuracy, which is valuable when one is exploring nanostructures that have not yet been fabricated. But direct application of the FEM to structures with plasmonic features can cause problems related to a truncation of the simulation domain [10].

Other approaches mentioned above are commonly known as semi-analytical methods. This means that one has already applied Green's theorem to the system of Maxwell equations [11] and reduced the scattering problem formulated in the whole of 3D space to the impurity domain. These methods can be divided into two kinds: the volume-based methods, similar to CDA and VIE, which are suitable for modeling of light scattering by arbitrary impurities; and the surface based methods, such as MMP, the T-matrix method and DSM. While volume-based methods can handle any kind of inhomogenities, they are pretty time-consuming, especially for the evaluation of integrated scattering characteristics. Surface-based methods seem to be more appropriate for the examination of homogeneous features deposited near an interface. Among others, the MMP and the DSM have several advantages. First of all they are semi-analytical meshless methods that do not require any integration procedure. The MMP and the DSM also provide a unique opportunity for a reliable validation of the results, as the errors can be calculated explicitly [5,7].

As is known, diverse practical applications in nano-optics, similar to optical antennas [12], photonic crystals [13], biosensors [14] and many others, require considering the simulation of scattering by features embedded in a stratified interface [15,16]. This leads to the necessity of accounting for multiple light reflections between a feature and the interface. The easiest way to handle this consists of incorporation of a green tensor (GT) of the stratified interface [17]. This can be done in the frame of both volume-based and surface-based methods [18–24]. For more than 15 years now, a Fresnel approximation of a GT (Image term) has been successfully employed to model a feature near an interface [25,26]. The MMP and the DSM have also been adjusted to incorporate GT and to consider many different kinds of nano-optical structures [19,20].

In the frame of the MMP or the DSM a scattered electromagnetic field is constructed as a finite linear combination of elementary sources: dipoles or multipoles, also called discrete sources (DS). Such representation satisfies all conditions of the scattering problem, except the transmission condition enforced at an obstacle surface. By satisfying these conditions one determines the amplitudes of the DS. Compared with the MMP the DSM has some specific features [20].

- It is focused on (but not restricted to) axial symmetric structures on or within a multilayered interface.
- It enables one to account for an axial symmetry by constructing a complete system of DS with minimal requirements.
- It allows one to account for the polarization of the external excitation (P or S).
- The positions of the DS can be adjusted to the singularities of the scattered field inside an obstacle by constructing the analytic continuation of the DS's coordinates into a complex plane.
- For fitting the transmission conditions at the obstacle surface, the Generalized Point-Matching Technique is used.
- The DSM incorporates Tikhonov's Regularization Technique in the least-square sense to obtain the DS amplitudes with a minimal norm.
- The DSM enables one to realize a convergence test by posterior error estimation.

In this paper we present two different applications of the DSM to light scattering problems of nano-optics. A detailed description of the problem itself as well as the mathematical statement and details of the numerical realization of the DSM-based models are presented in the corresponding chapters.

## 2. Light scattering by a nanoparticle in film

Enhanced optical transmission (EOT) through sub-wavelength holes in noble metal screens has attracted considerable interest since the discovery of this phenomenon in 1998 [27]. Wannemacher [28] has explained this effect by surface plasmon excitation. It is now generally agreed that surface plasmon resonances (SPR) play a key role in enhancement of light transmission through sub-wavelength apertures in thin noble metal screens [29–35]. This approach has already found a number of practical applications in nano-optics and biophotonics [36–37,14]. In most publications relating to this topic normal incidence of light onto the screen surface is considered. However, there are various practical applications based on evanescent wave scattering [38]. In particular, the use of evanescent excitation allows avoiding the problem of filtering the refracted wave behind the thin metal screen from the field scattered by a hole.

Recently the optical transmission through a nano-hole in the field of evanescent waves has been investigated by using the discrete sources method [38]. Extreme transmission effect (ETE) through a nano-sized cylindrical hole in thin noble film deposited by a glass prism has been detected by conducting computer simulation [39]. In the follow-up papers it was established that the ETE also occurs with other types of the film inhomogeneities [40,41]. The main ETE features consist of the following.

- The effect arises in the region of evanescent waves beyond the angle of total internal reflection for  $P$ -polarized external excitation.
- It demonstrates a sharp (by an order of magnitude) increase in the total scattering cross-section in the interval of  $1.5^\circ$  of the incident angle variation.
- It is independent of nano-sized inhomogeneity diameter, refractive index, film thickness or an external half-space material.
- It strongly depends on the noble film material.

In this section, the discrete sources method [38] has been adjusted to model polarized light scattering by a nano-sized particle located inside a noble metal film deposited on a glass prism. The scattering cross-sections in the upper and lower half-spaces as well as the signature of the differential scattering cross-section in the peak of ETE have been analyzed. Computer simulation shows a close correlation between ETE and surface plasmon resonance of the noble film [42]. In particular, the maximum of the ETE always just slightly varies from the maximum of the SPR (at  $0.03^\circ$ ). With a shift of the PSR peak, the ETE peak also shifts to nearly the same position.

In the next section we describe the mathematical problem and the scattering algorithm. Numerical results and discussion are presented in the final section.

### 2.1. Mathematical statement of the scattering problem

Let the whole space be divided into three domains: air  $D_0$ , film  $D_f$  and a glass prism, which is modeled as a half-space  $D_1$ . Let the plane  $\Sigma_1$  separate a film and a glass prism and the plane  $\Sigma_f$ , air and the film. An axial symmetric particle occupying a domain  $D_i$  with a smooth boundary  $\partial D_i$  is located inside the film of thickness  $d$ , bounded by the planes  $\Sigma_1$  and  $\Sigma_f$ . We assume that the symmetry axis of the particle coincides with the normal to  $\Sigma_1$ . Let us introduce a Cartesian coordinate system  $Oxyz$  by choosing its origin  $O$  at the prism-surface  $\Sigma_1$ . Let the  $Oz$  axis coincide with the symmetry axis of the particle and be directed into  $D_0$ . The plane  $z=0$  corresponds to the  $\Sigma_1$  plane (Figure 1). We assume that the exciting field  $\{\mathbf{E}^0, \mathbf{H}^0\}$  is a linear polarized plane wave propagating from the prism domain  $D_1$  at an angle  $\theta_1$  with respect to the  $Z$ -axis. Then the mathematical statement of the scattering problem can be written in the following form

$$\begin{aligned} \nabla \times \mathbf{H}_\zeta &= jk\varepsilon_\zeta \mathbf{E}_\zeta; \quad \nabla \times \mathbf{E}_\zeta = -jk\mu_\zeta \mathbf{H}_\zeta \text{ in } D_\zeta, \\ \zeta &= 0, f, 1, i, \quad \mathbf{n}_i \times \begin{cases} (\mathbf{E}_i(p) - \mathbf{E}_f(p)) = 0 \\ (\mathbf{H}_i(p) - \mathbf{H}_f(p)) = 0 \end{cases} \quad p \in \partial D_i, \\ \mathbf{e}_z \times \begin{cases} (\mathbf{E}_0(p) - \mathbf{E}_f(p)) = 0 \\ (\mathbf{H}_0(p) - \mathbf{H}_f(p)) = 0 \end{cases} \quad p \in \sum_f \end{aligned} \quad (1)$$

$$\lim_{r \rightarrow \infty} \left( \sqrt{\varepsilon_\zeta} \mathbf{E}_\zeta^s \times \frac{\mathbf{r}}{r} - \sqrt{\mu_\zeta} \mathbf{H}_\zeta^s \right) = 0, \quad r|M| \rightarrow \infty, \quad \zeta = 0, 1.$$

$$(|\mathbf{E}_f|, |\mathbf{H}_f|) = 0 (\exp\{-|\text{Im}k_f|\rho\}) \quad \rho = \sqrt{x^2 + y^2} \rightarrow \infty.$$

Here,  $\mathbf{n}_i$  is the outward unit normal vector to the surface  $\partial D_i$ ,  $k = \omega/c$ ,  $\{\mathbf{E}_\zeta, \mathbf{H}_\zeta\}$  stands for the total

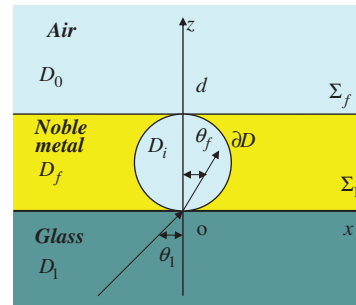


Figure 1. Model geometry: particle deposited in a film on surface. (The color version of this figure is included in the online version of the journal.)

and  $\{\mathbf{E}_\zeta^s, \mathbf{H}_\zeta^s\}$  stands for the scattered fields in the corresponding domain  $D_\zeta$ ,  $\mathbf{e}_z$  is the unit vector along the  $z$ -axis,  $\varepsilon_\zeta$  is the media permittivity and  $\mu_\zeta$  is the permeability,  $k_\zeta = k\sqrt{\varepsilon_\zeta\mu_\zeta}$ . If  $\text{Im}\varepsilon_\zeta, \mu_\zeta \leq 0$  (time dependence for the fields is chosen as  $\exp\{j\omega t\}$ ) and the particle surface is smooth enough,  $\partial D_i \subset C^{(2,\alpha)}$ , then the boundary-value problem (1) is uniquely solvable.

We start with the solution of the scattering problem of the plane wave  $\{\mathbf{E}^0, \mathbf{H}^0\}$  on the layered interface without the particle. The result yields the field of the external excitation  $\{\mathbf{E}_\zeta^0, \mathbf{H}_\zeta^0\}$ ,  $\zeta = 0, f, 1$  in all domains  $D_{0,f,1}$ , which satisfies the transmission conditions at the planes  $\Sigma_{1,f}$  [43]. While in  $D_{1,f}$  the exciting field consists of incident and reflected waves, in  $D_0$  the field includes the transmitted wave, which is transformed to the evanescent one behind a critical angle. In particular, the exciting field inside the film can be represented by a linear combination of plane waves propagating up and down inside the film, that is:

$$\begin{aligned} \mathbf{E}_f^0 &= w_i^{P,S} \mathbf{E}_f^{(+P,S)} + w_r^{P,S} \mathbf{E}_f^{(-P,S)}, \\ \mathbf{H}_f^0 &= w_i^{P,S} \mathbf{H}_f^{(+P,S)} + w_r^{P,S} \mathbf{H}_f^{(-P,S)} \end{aligned} \quad (2)$$

where

$$\begin{aligned} \mathbf{E}_f^{(\pm)P} &= (\mp \cos \theta_f \mathbf{e}_x + \sin \theta_f \mathbf{e}_z) \chi^\pm; & \mathbf{H}_f^{(\pm)P} &= -n_f \mathbf{e}_y \chi^\pm \\ \mathbf{H}_f^{(\pm)S} &= n_f (\mp \cos \theta_f \mathbf{e}_x + \sin \theta_f \mathbf{e}_z) \chi^\pm; & \mathbf{E}_f^{(\pm)S} &= \mathbf{e}_y \chi^\pm \\ \chi^\pm &= \exp\{-jk_f(x \sin \theta_f \pm z \cos \theta_f)\}; \\ n_\zeta &= \sqrt{\varepsilon_\zeta \mu_\zeta}, \quad \zeta = 0, f, 1. \end{aligned}$$

$$w_i^{P,S} = \frac{t_{1f}^{P,S}}{1 - r_{f1}^{P,S} r_{f0}^{P,S} e_f^2}, \quad w_r^{P,S} = -r_{f0}^{P,S} e_f^2 w_i^{P,S},$$

$$e_f = \exp\{-jk_f d \cos \theta_f\}.$$

Here,  $r_{\alpha\beta}^{P,S}, t_{\alpha\beta}^{P,S}$  are the corresponding coefficients of reflection and transmission at the interface between the  $D_\alpha$  and  $D_\beta$  domains, for  $P$ - and  $S$ -polarized plane waves [43]

$$\begin{aligned} r_{\alpha\beta}^P &= \frac{n_\alpha \cos \theta_\beta - n_\beta \cos \theta_\alpha}{n_\alpha \cos \theta_\beta + n_\beta \cos \theta_\alpha}, & t_{\alpha\beta}^P &= \frac{2n_\alpha \cos \theta_\alpha}{n_\alpha \cos \theta_\beta + n_\beta \cos \theta_\alpha}, \\ r_{\alpha\beta}^S &= \frac{n_\alpha \cos \theta_\alpha - n_\beta \cos \theta_\beta}{n_\alpha \cos \theta_\alpha + n_\beta \cos \theta_\beta}, & t_{\alpha\beta}^S &= \frac{2n_\alpha \cos \theta_\alpha}{n_\alpha \cos \theta_\alpha + n_\beta \cos \theta_\beta}, \end{aligned} \quad (3)$$

$\theta_f$  is a transmission angle according to Snell's law,  $n_\zeta = \sqrt{\varepsilon_\zeta \mu_\zeta}$  is the corresponding refractive index,  $\mathbf{e}_{x,y,z}$  is an orthogonal Cartesian basis.

The advantage of the DSM is that it is a semi-analytical meshless method and it does not require any integration procedure. In the frame of DSM [7],

the approximate solution is constructed by representing the electromagnetic fields as a finite linear combination of the electric and magnetic fields of dipoles and multipoles, which are distributed over the axis of symmetry inside the particle or in an adjoined complex plane. In addition, the fields of the dipoles and multipoles analytically satisfy the transmission conditions enforced at the plane interfaces  $\Sigma_{1,f}$ . This circumstance plays a key role for it analytically provides an opportunity to account for all interactions caused by multiple fields' reflections between the particle and the interfaces. Then the DSM approximate solution satisfies Maxwell equations in the domains  $D_\zeta$ ,  $\zeta = 0, 1, f, i$ , the required infinity conditions and the transmission conditions enforced at the plane interfaces  $\Sigma_{1,f}$ . Thus, the scattering problem (1) is reduced to the problem of approximation of an exciting field  $\{\mathbf{E}_f^0, \mathbf{H}_f^0\}$  at the particle's surface  $\partial D_i$ . Only the amplitudes of the discrete sources (DS) are to be determined from the boundary conditions at  $\partial D_i$ , which accept the following form:

$$\begin{aligned} \mathbf{n}_i \times (\mathbf{E}_f(p) - \mathbf{E}_f^0(p)) &= \mathbf{n}_i \times \mathbf{E}_f^0(p), \\ \mathbf{n}_i \times (\mathbf{H}_f(p) - \mathbf{H}_f^0(p)) &= \mathbf{n}_i \times \mathbf{H}_f^0(p), \end{aligned} \quad p \in \partial D_i. \quad (4)$$

## 2.2. Construction of an approximate solution

To construct the fields of electric and magnetic dipoles and multipoles that analytically satisfy the transmission conditions at the plane interfaces  $\Sigma_{1,f}$  we incorporate Green's tensor for a layered interface [43]:

$$\overset{\leftrightarrow}{\mathbf{G}}(M, M_0) = \begin{bmatrix} G_{11}^{e,h} & 0 & 0 \\ 0 & G_{11}^{e,h} & 0 \\ \partial F^{e,h}/\partial x_M & \partial F^{e,h}/\partial y_M & G_{33}^{e,h} \end{bmatrix} \quad (5)$$

where the components of the Green tensor (5) can be written as:

$$\begin{aligned} G_{11}^{e,h}(M, M_0) &= \int_0^\infty J_0(\lambda r) v_{11}^{e,h}(\lambda, z, z_0) \lambda \, d\lambda \\ G_{33}^{e,h}(M, M_0) &= \int_0^\infty J_0(\lambda r) v_{33}^{e,h}(\lambda, z, z_0) \lambda \, d\lambda \\ F^{e,h}(M, M_0) &= \int_0^\infty J_0(\lambda r) v_{31}^{e,h}(\lambda, z, z_0) \lambda \, d\lambda. \end{aligned} \quad (6)$$

Here  $R_{M,M_0}^2 = r^2 + (z - z_0)^2$ ,  $r^2 = \rho^2 + \rho_0^2 - 2\rho\rho_0 \cos(\varphi - \varphi_0)$ ,  $J_0(\cdot)$  is a cylindrical Bessel function of zero order, and  $(\rho, \varphi, z)$  are cylindrical coordinates of the  $M$  point. For the spectral functions  $v_{11}^{e,h}(z, z_0, \lambda)$ ,  $v_{33}^{e,h}(z, z_0, \lambda)$ ,  $v_{31}^{e,h}(z, z_0, \lambda)$  which satisfy the transmission

conditions at  $z=0, d$  the following representations are valid

$$v_{11}^{e,h}(z, z_0, \lambda) = \begin{cases} A_{11}^{e,h}(\lambda, z_0, d) \exp\{-\eta_0|z-d|\}, & z > d \\ \frac{\exp\{-\eta_f|z-z_0|\}}{\eta_f} + B_{11}^{e,h} \exp\{-\eta_f|z-d|\} \\ \quad + C_{11}^{e,h} \exp\{-\eta_f z\}, & d > z > 0 \\ D_{11}^{e,h}(\lambda, z_0, d) \exp\{-\eta_1 z\}, & z < 0 \end{cases}$$

$$v_{33}^{e,h}(z, z_0, \lambda) = \begin{cases} A_{33}^{e,h}(\lambda, z_0, d) \exp\{-\eta_0|z-d|\}, & z > d \\ \frac{\exp\{-\eta_f|z-z_0|\}}{\eta_f} B_{33}^{e,h} \exp\{-\eta_f|z-d|\} \\ \quad + C_{33}^{e,h} \exp\{-\eta_f z\}, & d > z > 0 \\ D_{33}^{e,h}(\lambda, z_0, d) \exp\{-\eta_1 z\}, & z < 0 \end{cases}$$

$$v_{31}^{e,h}(z, z_0, \lambda) = \begin{cases} A_{31}^{e,h}(\lambda, z_0, d) \exp\{-\eta_0|z-d|\}, & z > d \\ B_{31}^{e,h}(\lambda, z_0, d) \exp\{-\eta_f|z-d|\} \\ \quad + C_{31}^{e,h}(\lambda, z_0, d) \exp\{-\eta_f z\}, & d > z > 0 \\ D_{31}^{e,h}(\lambda, z_0, d) \exp\{\eta_1 z\}, & z < 0. \end{cases} \quad (7)$$

Here

$$\eta_\zeta^2 = \lambda^2 - k_\zeta^2, \quad k_\zeta^2 = k^2 \varepsilon_\zeta \mu_\zeta, \quad \zeta = 0, f, 1.$$

The associated spectral coefficients  $A_{\alpha\beta}^{e,h}, B_{\alpha\beta}^{e,h}, C_{\alpha\beta}^{e,h}, D_{\alpha\beta}^{e,h}$  are determined from the following conditions at  $z=0, d$ :

$$[v_{11}^e] = \left[ \frac{1}{\mu} \frac{\partial v_{11}^e}{\partial z} \right] = 0; \quad [v_{11}^h] = \left[ \frac{1}{\varepsilon} \frac{\partial v_{11}^h}{\partial z} \right] = 0;$$

$$\left[ \frac{1}{\mu} v_{31}^e \right] = 0; \quad \left[ \frac{1}{\varepsilon \mu} \frac{\partial v_{31}^e}{\partial z} \right] = - \left[ \frac{1}{\varepsilon \mu} \right] v_{11}^e, \quad \left[ \frac{1}{\varepsilon} v_{31}^h \right] = 0;$$

$$\left[ \frac{1}{\varepsilon \mu} \frac{\partial v_{31}^h}{\partial z} \right] = - \left[ \frac{1}{\varepsilon \mu} \right] v_{11}^h. \quad (8)$$

Here, square brackets  $[\cdot]$  stay for change of values at the interface.

In frame of the DSM, the approximate solution of the scattering problem is constructed accounting for rotational symmetry of the scattering problem geometry (particle together with layered interface). In this case, the DS are distributed over the axis of symmetry and the Fourier harmonics of the Green tensor components (Equation (6)) are used to build the solution. The Fourier harmonics  $g_m^{e,h}, f_m$  accept the

form of Weyl–Sommerfeld integrals:

$$g_m^{e,h}(q, w_n) = \int_0^\infty J_m(\lambda \rho) v_{11}^{e,h}(z, w_n, \lambda) \lambda^{1+m} d\lambda,$$

$$f_m^{e,h}(q, w_n) = \int_0^\infty J_m(\lambda \rho) v_{31}^{e,h}(z, w_n, \lambda) \lambda^{1+m} d\lambda. \quad (9)$$

Here,  $J_m(\cdot)$  is the cylindrical Bessel function, and the multipoles are distributed along the axis of symmetry  $w_n \in Oz$  inside  $D_i$  or in an adjoined complex plane by setting  $w = z' \pm jz''$  as it was introduced in [44].

In addition to the axial symmetry, the polarization of the exciting field is also taken into account during the approximate solution construction [7]. Let us now consider a  $P$ -polarized excitation (Equation (2)). To account for the axial symmetry and polarization of the exciting field we implement a plane wave resolution into a Fourier series with respect to the azimuth angle  $\varphi$ :

$$\exp\{-jk_f \rho \sin \theta_f \cos \varphi\} = \sum_{m=0}^{\infty} (2 - \delta_{0m}) (-j)^m \times J_m(k_f \rho \sin \theta_f) \cos m\varphi. \quad (10)$$

Here,  $\delta_{0m}$  is a Kronecker symbol. Then for the associated Fourier harmonics of the external excitation in the cylindrical coordinate system the following representations hold:

$$\mathbf{E}_f^P(m) = \{ \mathbf{E}_{m\rho}^P(q) \cos(m+1)\varphi; \quad \mathbf{E}_{m\varphi}^P(q) \sin(m+1)\varphi; \\ \mathbf{E}_{mz}^P(q) \cos(m+1)\varphi \}$$

$$\mathbf{H}_f^P(m) = \{ \mathbf{H}_{m\rho}^P(q) \sin(m+1)\varphi; \quad \mathbf{H}_{m\varphi}^P(q) \cos(m+1)\varphi; \\ \mathbf{H}_{mz}^P(q) \sin(m+1)\varphi \} \quad (11)$$

where  $q = (\rho, z)$  stands for a point located in the half-plane  $\varphi = \text{const}$ . To take the polarization of the external excitation into account we use a linear combination of electrical and magnetic multipoles positioned along the axis of symmetry, which are adjusted to the external excitation (Equation (11)) [7]. For the representation of the scattered field outside the particle the following vector potentials are used:

$$\mathbf{A}_{nm}^{e,f} = \{ g_m^e(q, w_n) \cos(m+1)\varphi; \quad -g_m^e(q, w_n) \sin(m+1)\varphi; \\ -f_{m+1}(q, w_n) \cos(m+1)\varphi \},$$

$$\mathbf{A}_{nm}^{h,f} = \{ g_m^h(q, w_n) \sin(m+1)\varphi; \quad g_m^h(q, w_n) \cos(m+1)\varphi; \\ -f_{m+1}(q, w_n) \sin(m+1)\varphi \},$$

$$\mathbf{A}_{0n}^{e,f} = \{ 0; \quad 0; \quad g_0^h(q, w_n) \}. \quad (12)$$

The total field inside the particle is constructed based on vector potentials, which have the form [7]:

$$\begin{aligned}\mathbf{A}_{mn}^{e,i} &= \{Y_m(q, w_n^i) \cos(m+1)\varphi; \\ &\quad - Y_m(q, w_n^i) \sin(m+1)\varphi; \quad 0\} \\ \mathbf{A}_{mn}^{h,i} &= \{Y_m(q, w_n^i) \sin(m+1)\varphi; \\ &\quad Y_m(q, w_n^i) \cos(m+1)\varphi; \quad 0\} \\ \mathbf{A}_{0n}^{e,i} &= \{0; \quad 0; \quad Y_0(q, w_n^i)\}.\end{aligned}\quad (13)$$

Here,  $Y_m(a, w_n^i) = h_m^{(2)}(k_i R_{qw_n^i}) \cdot (k_i \rho / R_{qw_n^i})^m$ ,  $R_{qw_n^i} = \sqrt{\rho^2 + (z - w_n^i)^2}$  and  $h_m^{(2)}(\cdot)$  are spherical Hankel functions. Let us emphasize that the sets  $\{w_n^i\}$  and  $\{w_n\}$  are different because  $w_n^i$  must be placed outside of  $D_i$ .

Thus, for the scattered fields in  $D_0, f, 1$ , which satisfy the transmission conditions at  $\Sigma_{1,f}$  and the total field inside  $D_i$ , the following representation is valid:

$$\begin{aligned}\mathbf{E}_{\zeta, N}^{\zeta} &= \sum_{m=0}^M \sum_{n=1}^{N_m^{\zeta}} \left\{ p_{mn}^{\zeta} \frac{j}{k \varepsilon_{\zeta} \mu_{\zeta}} \nabla \times \nabla \times \mathbf{A}_{mn}^{e, \zeta} + q_{mn}^{\zeta} \frac{1}{\varepsilon_{\zeta}} \nabla \times \mathbf{A}_{mn}^{h, \zeta} \right\} \\ &\quad + \sum_{n=1}^{N_0^{\zeta}} r_n^{\zeta} \frac{j}{k \varepsilon_{\zeta} \mu_{\zeta}} \nabla \times \nabla \times \mathbf{A}_{0n}^{e, \zeta}, \\ \mathbf{H}_{\zeta, N}^{\zeta} &= \frac{j}{k \mu_{\zeta}} \nabla \times \mathbf{E}_{\zeta, N}^{\zeta}(M), \quad \zeta = 0, f, 1, i; \quad \zeta = f, i.\end{aligned}\quad (14)$$

Let us emphasize that the representations for the scattered fields in three domains  $D_0, f, 1$  are provided by the unique set of amplitudes  $\{p_{mn}^f, q_{mn}^f, r_n^f\}$ .

The approximate solution for  $S$ -polarized excitation can be constructed in a similar way. Accounting for the Fourier harmonics of an exciting wave, the formulation (2) can be written as follows:

$$\begin{aligned}\mathbf{E}_{f(m)}^S &= \{\mathbf{E}_{m\rho}^S(q) \sin(m+1)\varphi; \quad \mathbf{E}_{m\varphi}^S(q) \cos(m+1)\varphi; \\ &\quad \mathbf{E}_{mz}^S(q) \sin(m+1)\varphi\} \\ \mathbf{H}_{f(m)}^S &= \{\mathbf{H}_{m\rho}^S(q) \cos(m+1)\varphi; \quad \mathbf{H}_{m\varphi}^S(q) \sin(m+1)\varphi; \\ &\quad \mathbf{H}_{mz}^S(q) \cos(m+1)\varphi\}.\end{aligned}\quad (15)$$

Here, the following electric and magnetic vector potentials corresponding to the dipoles and multipoles are employed:

$$\begin{aligned}\mathbf{A}_{mn}^{e,f} &= \{g_m^e(q, w_n) \sin(m+1)\varphi; \quad g_m^e(q, w_n) \cos(m+1)\varphi; \\ &\quad -f_{m+1}(q, w_n) \sin(m+1)\varphi\}, \\ \mathbf{A}_{mn}^{h,f} &= \{g_m^h(q, w_n) \cos(m+1)\varphi; \quad -g_m^h(q, w_n) \sin(m+1)\varphi; \\ &\quad -f_{m+1}(q, w_n) \cos(m+1)\varphi\}, \\ \mathbf{A}_{0n}^{h,f} &= \{0; \quad 0; \quad g_0^e(q, w_n)\}.\end{aligned}\quad (16)$$

The vector potentials for the total field inside the particle accept the form

$$\begin{aligned}\mathbf{A}_{mn}^{e,i} &= \{Y_m(q, w_n^i) \sin(m+1)\varphi; \\ &\quad - Y_m(q, w_n^i) \cos(m+1)\varphi; \quad 0\} \\ \mathbf{A}_{mn}^{h,i} &= \{Y_m(q, w_n^i) \cos(m+1)\varphi; \\ &\quad Y_m(q, w_n^i) \sin(m+1)\varphi; \quad 0\}; \\ \mathbf{A}_{0n}^{h,i} &= \{0; \quad 0; \quad Y_0(q, w_n^i)\}.\end{aligned}\quad (17)$$

Then, for the scattered fields in  $D_0, 1, f$ , which satisfy the transmission conditions at both interfaces  $\Sigma_{1,f}$  and the total field inside the particle  $D_i$ , the following representation is valid:

$$\begin{aligned}\mathbf{E}_{\zeta, N}^{\zeta} &= \sum_{m=0}^M \sum_{n=1}^{N_m^{\zeta}} \left\{ p_{mn}^{\zeta} \frac{j}{k \varepsilon_{\zeta} \mu_{\zeta}} \nabla \times \nabla \times \mathbf{A}_{mn}^{e, \zeta} + q_{mn}^{\zeta} \frac{1}{\varepsilon_{\zeta}} \nabla \times \mathbf{A}_{mn}^{h, \zeta} \right\} \\ &\quad + \sum_{n=1}^{N_0^{\zeta}} r_n^{\zeta} \frac{j}{k \varepsilon_{\zeta} \mu_{\zeta}} \nabla \times \mathbf{A}_{mn}^{h, \zeta}, \\ \mathbf{H}_{\zeta, N}^{\zeta} &= \frac{j}{k \mu_{\zeta}} \nabla \times \mathbf{E}_{\zeta, N}^{\zeta}(M), \quad \zeta = 0, f, 1, i; \quad \zeta = f, i.\end{aligned}\quad (18)$$

The following result holds: let each set  $\{w_n\}_{n=1}^{\infty}, \{w_n^i\}_{n=1}^{\infty}$  have at least one limit point. Then the systems of dipoles and multipoles are complete in the least square sense on  $\partial D_i$  and the constructed approximate solutions (14) and (18) of the scattering problem (1) converge to the exact one [38].

The system of multipoles that has been used for representation of the fields is called the lowest order multipoles [6].

### 2.3. Numerical scheme of the DSM

In this section, a short description of the numerical scheme of the DSM is presented. As mentioned above, the representations (14) and (18) satisfy all the conditions of the scattering problem (1) except for the transmission conditions at the particle's surface (4). These transmission conditions are used to determine the unknown amplitudes of the DS  $\{p_{mn}^{\zeta}, q_{mn}^{\zeta}, r_n^{\zeta}\}; m = 0, M; n = 1, N; \zeta = f, i$ . Note that for each Fourier harmonic  $m$  we have to compute the coefficients  $\{p_{mn}^f, q_{mn}^f, r_n^f\}_{n=1}^{N_m^f}$  and  $\{p_{mn}^i, q_{mn}^i, r_n^i\}_{n=1}^{N_m^i}$  only, because by using Green's tensor we constructed a unitary representation of the fields outside  $D_i$  with the same amplitudes.

Let us remind ourselves that the geometry of our scattering problem is axially symmetric with respect to the  $Z$ -axis and the DS are distributed over its axis of symmetry. To account for the singularities of the

continuation of the scattered field inside the particle we construct an analytic continuation of the DS's coordinates to the adjoined complex plane  $\{w_n\}_{n=1}^{N_m^f}$  [7]. The DS used for the internal field representation  $\{w_n^i\}_{n=1}^{N_m^i}$  are placed in the complex plane in such a way that their projections to the real axis ( $Oz$ ) do not touch the internal domain  $D_i$ . In this case the representation for internal fields accepts the form of a finite Fourier series with respect to the azimuth variable  $\varphi$ . By resolving the fields of the exciting plane waves (Equation (2)) in the Fourier series we transform the surface approximation problem (Equation (4)) to a set of one-dimensional approximating problems for the fields (see Equations (11)–(14) for  $P$ -polarization or Equations (15)–(18) for  $S$ -polarization) enforced at the particle meridian [7]. Thus, instead of matching the fields over the whole scattering surface, their Fourier harmonics are matched separately. By resolving this problem the corresponding DS amplitudes  $\{p_{nm}^\zeta, q_{nm}^\zeta, r_n^\zeta\}$ ;  $\zeta = f, i$  are determined. Additionally, the DSM allows employment of different numbers of DS for representations of the scattered and the internal fields, which enables examination of particles with high refractive indices.

There are various numerical schemes for the evaluation of the DS's amplitudes. It has been found that the most stable results can be obtained by using the Generalized Point-Matching (GPM) Technique. The GPM requires distribution of the matching points  $\{\rho_l, z_l\}_{l=1}^L$  over the generatrix covering its whole length. GPM provides a considerable reduction of sizes of linear systems involved and leads to reduction of the computational time and memory storage, due to the possibility of using a lower DS number compared with the number of matching points. To provide the fullness of rank of the rectangular matrices for each Fourier harmonic in the over-determined systems, the Tikhonov's regularization procedure in least square form is applied [38] with a spectral shift in a complex plane. The amplitudes of multipoles are then determined as a pseudo-solution of the corresponding over-determined system of linear equations [7].

Usually, the number of DS we use ( $N_m^f + N_m^i$ ) depends on the number of Fourier harmonics  $m$  and takes on a value up to half the number of the matching points distributed over  $\mathfrak{J}$ . Additionally, we make a separation between the number of DS for the scattered field  $N_m^f$  and for the internal one  $N_m^i$  depending on the values of the refractive indices of the particle and the film. The higher the value of the refractive index the higher the number of DS required. The latter circumstance allows examining

a particle with a high refractive index. Thus, the matrix dimension for a Fourier harmonic is  $4L \times (2N_m^f + 2N_m^i)$ .

Because the DSM is a direct method, it does not require any iterative solver. Regardless, we use different representations for  $P$ - (Equation (14)) and  $S$ - (Equation (18)) polarized excitation, and it has been shown that the DS amplitudes can be determined by solving a linear system with an identical matrix for both  $P$ - and  $S$ - cases [7]. The last fact allows solving the scattering problem for the complete set of incident angles  $\theta_1$  and both polarizations ( $P$  and  $S$ ) at once. In addition, the DSM numerical scheme provides an opportunity to control the actual convergence of the approximate solution to the exact one by posterior error estimation. For this purpose, we calculate a surface residual of the transmission conditions (Equation (3)) in least square norm at  $\partial D_i$  [7].

After the Fourier harmonics of the DS amplitudes are determined, one can compute the far field patterns  $\mathbf{F}_{0,1}(\theta, \varphi)$  in  $D_{0,1}$  domains:

$$\mathbf{E}_{0,1}^s(M)/|\mathbf{E}^0(z=0)| = \frac{\exp\{-jk_{0,1}r\}}{r} \mathbf{F}_{0,1}(\theta, \varphi) + 0(r^{-1}),$$

$$r = |M| \rightarrow \infty. \quad (19)$$

Here  $\mathbf{F}_{0,1}(\theta, \varphi)$  are determined at a unit sphere and have two components corresponding to  $P/S$  polarized excitation  $\mathbf{F}_{0,1}^{P,S}(\theta, \varphi) = \mathbf{F}_{0,1(\theta)}^{P,S} \mathbf{e}_\theta + \mathbf{F}_{0,1(\varphi)}^{P,S} \mathbf{e}_\varphi$ .

By asymptotical evaluation of the Weyl–Sommerfeld integrals involved in the representation of the scattered fields, the far field pattern components for  $P$ -polarization accept the following form [45]:

$$F_{0,1(\theta)}^P(\theta, \varphi) = jk \sum_{m=0}^M (jk_{0,1} \sin \theta)^m \cos(m+1)\varphi$$

$$\times \sum_{n=1}^{N_m^f} \left\{ p_{nm}^{f,P} [\bar{g}_{nm}^{e(0,1)} \cos \theta + jk_{0,1} \sin^2 \theta \bar{f}_{nm}^{e(0,1)}] \right.$$

$$\left. + \sqrt{\frac{\mu_{0,1}}{\varepsilon_{0,1}}} q_{nm}^{f,P} \bar{g}_{nm}^{-h(0,1)} \right\} - jk \sin \theta \sum_{n=1}^{N_0^f} r_n^{f,P} \bar{g}_{n0}^{-h(0,1)},$$

$$F_{0,1(\varphi)}^P(\theta, \varphi) = -jk \sum_{m=0}^M (jk_{0,1} \sin \theta)^m \sin(m+1)\varphi$$

$$\times \sum_{n=1}^{N_m^f} \left\{ p_{nm}^{f,P} \bar{g}_{nm}^{-e(0,1)} + \sqrt{\frac{\mu_{0,1}}{\varepsilon_{0,1}}} q_{nm}^{f,P} [\bar{g}_{nm}^{h(0,1)} \cos \theta \right.$$

$$\left. + jk_{0,1} \sin^2 \theta \bar{f}_{nm}^{h(0,1)} \right\}. \quad (20)$$

For  $S$ -polarized external excitation the components of the far field pattern are

$$\begin{aligned}
 F_{0,1(\theta)}^S(\theta, \varphi) &= jk \sum_{m=0}^M (jk_{0,1} \sin \theta)^m \sin(m+1)\varphi \\
 &\times \sum_{n=1}^N \left\{ p_{nm}^{f,S} \left[ \bar{g}_{nm}^{e(0,1)} \cos \theta + jk_{0,1} \sin^2 \theta \bar{f}_{nm}^{e(0,1)} \right] \right. \\
 &\quad \left. - \sqrt{\frac{\mu_{0,1}}{\varepsilon_{0,1}}} q_{nm}^{f,S} \bar{g}_{nm}^{h(0,1)} \right\}, \\
 F_{0,1(\varphi)}^S(\theta, \varphi) &= jk \sum_{m=0}^M (jk_{0,1} \sin \theta)^m \cos(m+1)\varphi \\
 &\times \sum_{n=1}^N \left\{ p_{nm}^{f,S} \bar{g}_{nm}^{e(0,1)} - \sqrt{\frac{\mu_{0,1}}{\varepsilon_{0,1}}} q_{nm}^{f,S} \left[ \bar{g}_{nm}^{h(0,1)} \cos \theta \right. \right. \\
 &\quad \left. \left. + jk_{0,1} \sin^2 \theta \bar{f}_{nm}^{h(0,1)} \right] \right\} \\
 &+ jk \sqrt{\frac{\mu_{0,1}}{\varepsilon_{0,1}}} \sin \theta \sum_{n=1}^N r_n^{f,S} \bar{g}_{nm}^{h(0,1)}, \quad (21)
 \end{aligned}$$

here,  $\{p_{nm}^{f,(P,S)}, q_{nm}^{f,(P,S)}, r_n^{f,(P,S)}\}$  are Fourier harmonics of DS amplitudes corresponding to  $P/S$  polarizations and the associating spectral functions  $\bar{g}_{nm}^{e,h}, \bar{f}_{nm}$  are

$$\begin{aligned}
 \bar{g}_{nm}^{e,h(0)}(\theta) &= jk_0 \cos \theta \exp\{jk_0 d \cos \theta\} A_{11}^{e,h}(k_0 \sin \theta, w_n, d), \\
 \bar{f}_{nm}^{e,h(0)}(\theta) &= jk_0 \cos \theta \exp\{jk_0 d \cos \theta\} A_{31}^{e,h}(k_0 \sin \theta, w_n, d). \\
 \bar{g}_{nm}^{e,h(1)} &= jk_1 \cos \theta D_{11}^{e,h}(k_1 \sin \theta, w_n, d) \\
 \bar{f}_{nm}^{e,h(1)} &= jk_1 \cos \theta D_{31}^{e,h}(k_1 \sin \theta, w_n, d) \quad (22)
 \end{aligned}$$

where  $w_n$  denotes complex coordinates of the DS.

Hence, after the unknown amplitudes of DS are determined, the far field patterns for  $P/S$  polarization (Equations (20) and (21)) are represented as finite linear combinations of elementary functions. This circumstance ensures a low costs computer analysis of the scattering characteristics in the far zone.

## 2.4. Numerical results and discussion

In this section we consider several scattering characteristics. First, the differential scattering cross-section (DSC), in  $D_{0,1}$ , which is calculated as:

$$DSC_{0,1}^{P,S}(\theta_1, \theta, \varphi) = \left| F_{0,1(\theta)}^{P,S}(\theta_1, \theta, \varphi) \right|^2 + \left| F_{0,1(\varphi)}^{P,S}(\theta_1, \theta, \varphi) \right|^2, \quad (23)$$

where  $F_{0,1(\varphi)}^{P,S}(\theta_1, \theta, \varphi)$  are the components of the far field pattern for a  $P$ - and  $S$ -polarized incident wave, in a spherical coordinate system  $\theta, \varphi$  (see Equations (16) and (17)).

We also consider the scattering cross-section (SCS), which represents the total integrated intensity scattered into the upper  $\Omega_0 = \{0^\circ \leq \theta \leq 90^\circ, 0^\circ \leq \varphi \leq 360^\circ\}$  and lower  $\Omega_1 = \{90^\circ \leq \theta \leq 180^\circ, 0^\circ \leq \varphi \leq 360^\circ\}$  hemispheres

$$\sigma_{0,1}^{P,S}(\theta_1) = \int_{\Omega_{0,1}} I_{0,1}^{P,S}(\theta_1, \theta, \varphi) d\omega. \quad (24)$$

Let  $\theta_0$  be a transmission angle of the exciting plane wave in  $D_0$ . Snell's law in this case yields:  $\sin \theta_0 = \frac{n_1}{n_0} \sin \theta_1$ . As  $|n_1| > |n_0|$  with an increase of the incident angle  $\theta_1$  from 0 to  $\pi/2$  one can get  $|\sin \theta_0| > 1$ . This circumstance requires using a corresponding branch for  $\cos \theta_0 = -j\sqrt{\sin^2 \theta_0 - 1}$ , which provides the choice of an outgoing wave. Hence, beyond the critical angle  $\theta_c = \arcsin(n_0/n_1)$  in the upper half-space an evanescent wave appears, which propagates along the interface and decays in the normal ( $z > d$ ) direction to the interface  $\Sigma_f$ :

$$\chi^+ = \exp\{-jk_0 x \sin \theta_0\} \exp\left\{-k_0 z \sqrt{\sin^2 \theta_0 - 1}\right\}.$$

Next, we will present some numerical results obtained by using the DSM model and discuss them. We consider  $P$ - or  $S$ -polarized plane waves with a wavelength of  $\lambda = 633$  nm. The prism is made of glass. The spherical silicon particle with diameter  $D = 49$  nm and a refractive index of  $n_i = 4.37 - 0.08j$  is embedded into a gold film of thickness  $d = 50$  nm with a refractive index for this wavelength  $n_f = 0.18 - 3.26j$ .

We will investigate the SCS both above the film in the area  $D_0$  and in the prism area  $D_1$ .

In Figure 2 the numerical results for the  $\sigma_{0,1}^{P,S}(\theta_1)$  of the particle versus scattered angle are presented in logarithmic scale. The glass prism refractive index is  $n = 1.904$  and the critical angle is equal to  $\theta_c = 31.68^\circ$ .

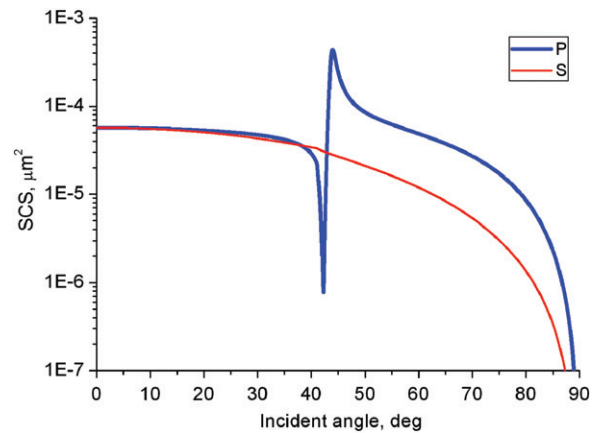


Figure 2. Si particle of  $D = 49$  nm in gold film  $d = 50$  nm on the prism  $n = 1.904$ , intensity above the film. (The color version of this figure is included in the online version of the journal.)

One can observe that while the SCS for *S*-polarized excitation monotonically decreases, the curve for *P*-polarized light has some special feature. Near the critical angle it has a sharp minimum and behind the critical angle it sharply rises in value up to two orders in magnitude. This effect occurs in the evanescent wave area. It was first time detected in [39] for a hole inside a film and we called it the extreme transmission effect (ETE).

In Figure 3 results for the same particle but for the SCS observed in  $D_0$  and in  $D_1$  separately are presented in linear scale. A closer look shows that the behavior of the SCS curves for both above and beneath the film are similar: curves for *S*-polarization demonstrate just a monotonic decrease of values, while both curves for *P*-polarized excitation first drop down and then sharply jump up in the area of evanescent waves. The curves demonstrate an increase of values at the angle variation of  $1.5^\circ$ .

Similar results are presented in Figure 4 for another prism material: glass with a refractive index of  $n = 1.52$ . Due to the shift of the critical angle of the system, the effect is also shifted to the critical angle  $\theta_c = 41.14^\circ$ , but the behavior of curves looks similar to the results presented in Figure 3. For a better illustration of this shift, the results for *P*-polarized excitation both above and beneath the film for the two different prism materials mentioned above are presented in Figure 5.

Let us consider a correlation between ETE and surface plasmon resonance (SPR) [42]. As is known, the SPR corresponds to a minimum value of the reflection  $R_{01}^P$  from the prism-film interface for a *P*-polarized plane wave. SPR appears behind the angle of total internal reflection  $\theta_1 > \theta_c$

$$R_{01}^P(\theta_1) = \frac{r_{1f}^P r_{f0}^P \exp\{-2jk_f \cos \theta_f d\}}{1 + r_{1f}^P r_{f0}^P \exp\{-2jk_f \cos \theta_f d\}}. \quad (25)$$

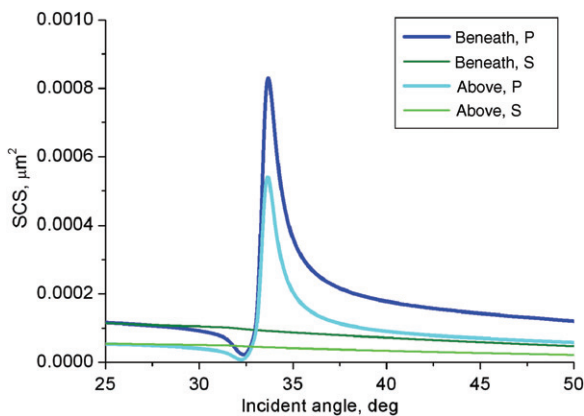


Figure 3. Particle in gold film on the prism  $n=1.904$ , *P*- and *S*-polarized excitations, intensities above and beneath the film. (The color version of this figure is included in the online version of the journal.)

Here,  $r_{1f}, r_{f0}$  are the reflection coefficients (Equations (3)) from boundaries  $\Sigma_1, \Sigma_f$  and  $\theta_f$  is the angle of refraction into the film.

In Figure 6, results similar to those from Figure 5 can be observed for the case, when the upper half-space  $D_0$  is filled with water having a refractive index of  $n = 1.33$ . A variation of the refractive index leads to the shift of the critical angle  $\theta_c = 61.04^\circ$  and yields the shift of the maximal position for both curves. The maxima for the case of water becomes smoother and their values are lower. Besides, one can see a close correlation between SPR and ETE for both cases (air and water).

Similar results can be observed in Figure 7, where the results for SCS are shown for the glass with  $n = 1.52$  for both cases of air and water above the film.

Now we would like to examine the behavior of DSC in the incidence plane. For these investigations we

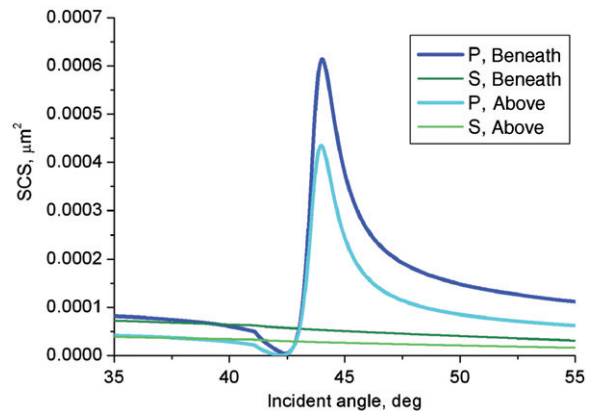


Figure 4. Particle in gold film on the prism  $n = 1.52$ , *P*- and *S*-polarized excitation, intensities above and beneath the film. (The color version of this figure is included in the online version of the journal.)

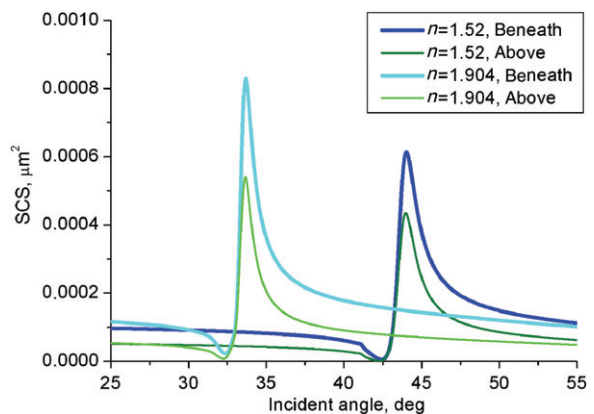


Figure 5. Particle in gold film, different prism materials, *P*-polarized excitation, intensities above and beneath the film. (The color version of this figure is included in the online version of the journal.)

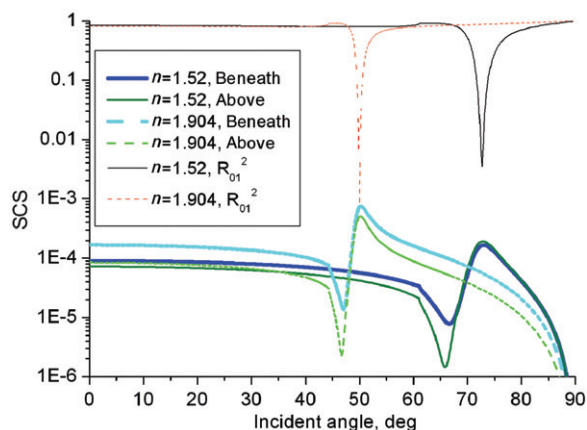


Figure 6. Particle in gold film, different prism materials,  $P$ -polarized excitation, water above. (The color version of this figure is included in the online version of the journal.)

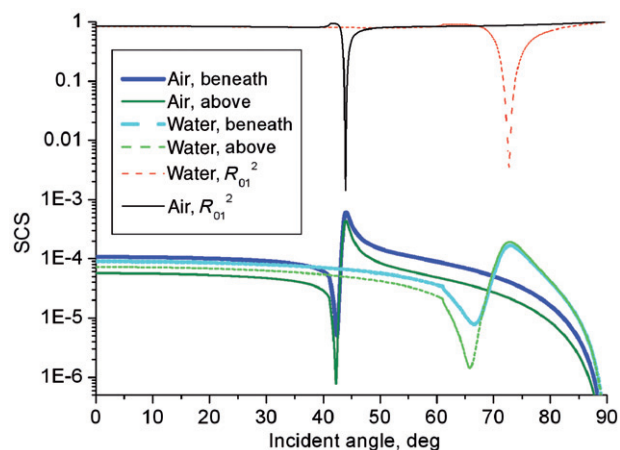


Figure 7. Particle in gold film on prism  $n=1.52$ ,  $P$ -polarization. (The color version of this figure is included in the online version of the journal.)

choose two incident angles, where the SCS demonstrates maximum and minimum values. The results for DSC distribution for the particle on glass with  $n=1.904$  are depicted in Figure 8 for both cases. Here the range of observation angles  $90^\circ < \theta < 270^\circ$  belongs to the upper semi-plane  $D_0$  and the range of  $270^\circ < \theta < 360^\circ$  belongs to the lower semi-plane  $D_1$ . Similar results are presented for another glass  $n=1.52$  in the case of air (Figure 9) above the film and in the case of water in  $D_0$  (Figure 10).

### 2.5. Conclusion

The extreme transmission effect arises in the region of evanescent waves behind the angle of total

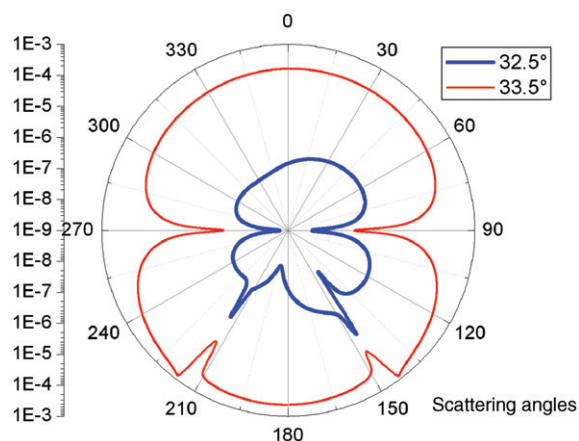


Figure 8. Particle in gold film on the prism  $n=1.904$ ,  $P$ -polarization. (The color version of this figure is included in the online version of the journal.)

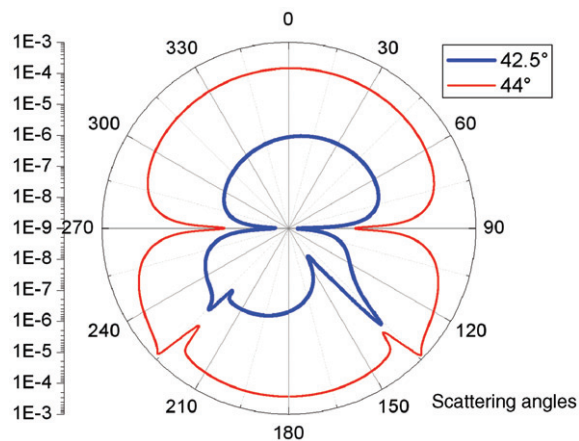


Figure 9. Particle in gold film on the prism  $n=1.52$ ,  $P$ -polarization. (The color version of this figure is included in the online version of the journal.)

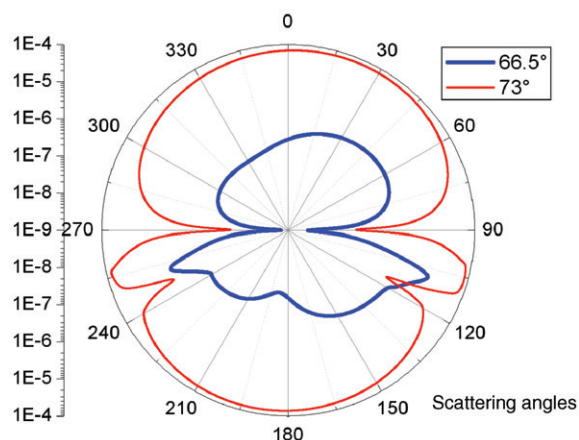


Figure 10. Particle in gold film on the prism  $n=1.52$ ,  $P$ -polarization, water above. (The color version of this figure is included in the online version of the journal.)

internal reflection. It demonstrates a sharp (by an order of magnitude) increase in the scattering cross-section compared with the normal incidence of the wave on the film. The spatial distribution of the scattered intensity in the peak of ETE has been analyzed. It was shown that SCS increases not only in the upper half-space  $D_0$  but also in the lower half-space  $D_1$ . The specific feature of this effect is that it is independent of the inhomogeneity shape, diameter and material, the film thickness, and the filling of the external half-space. Numerical results demonstrate close correlation of ETE with the surface plasmon resonance; in particular, the peaks of ETE correspond the peaks of SPR and always shift together with the shift of SPR peaks. In addition, the deviation of the ETE peak from SPR is about  $0.03^\circ$ .

### 3. Light scattering by particle on a filmed substrate for total internal reflection microscopy

Total internal reflection microscopy (TIRM) is a relatively new non-invasive technique to measure weak interaction forces between a single scattering colloidal particle and a plane surface with high resolution [46–50]. TIRM is an optical technique for monitoring the instantaneous separation distance between a microscopic particle and a flat surface. Variations of distance down to 1 nm can be detected. To determine the instantaneous separation distance, the intensity of light scattered by the sphere when it is illuminated by an evanescent wave is measured. Due to the use of the Brownian fluctuations of a free colloidal particle for obtaining the interaction potential, TIRM has a high sensitivity and is suitable for measurement close to a surface. In the last few years, TIRM has been applied to measure van der Waals [50], Casimir [51], magnetic [52], depletion [53,54], and electrostatic [55] forces.

The first TIRM measurements have been based on the assumption that the intensity of the scattered field out of the plane surface was proportional to the intensity of an evanescent field in the particle area. This assumption has been used for the reconstruction of the interaction potential. However, later experiments found a disagreement in behavior of measured interaction potentials for  $P$ - and  $S$ -polarized light with the original assumption [56]. The difference is caused by the particle–surface light scattering interaction, which has not been taken into consideration by the original simple model. To account for this scattering interaction, an exact scattering model, based on the discrete sources method has been suggested [57,58]. It has been shown that the use of the rigorous DSM model allows reconstruction of the interaction force potential with high precision [56–58].

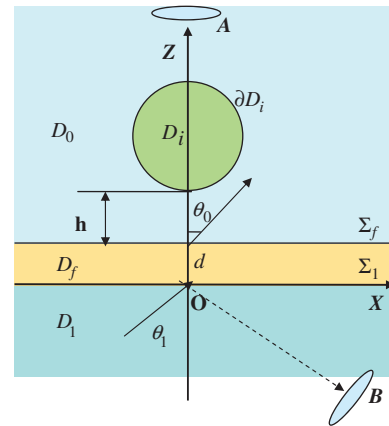


Figure 11. Model geometry: particle deposited on a filmed prism surface. (The color version of this figure is included in the online version of the journal.)

In a conventional TIRM setup, the colloidal particle is situated above the glass prism in a water-based medium. The laser beam propagating in the glass prism with an angle slightly higher than the angle of total internal reflection generates an evanescent field in the area above the prism. The light scattered by a colloidal particle is collected by a detector positioned in the liquid medium above the particle. Alternatively, it is possible to place the light collector in the area beneath the glass prism with the objective directed toward the specular beam. To reduce the intensity of the reflected beam the effect of surface plasmon resonance in a thin gold film, deposited on the prism surface is used.

In the present paper, the DSM is applied to model both setup schemes for TIRM. Numerical analysis based on the DSM model allows one to choose the most effective setup for determination of the particle–film distance. It has been found that placement of the collector beneath the prism is of advantage compared with its placement above the particle.

#### 3.1. Mathematical statement and solution construction

In this section we proceed with the mathematical statement of the scattering problem for the TIRM setup. Consider a glass prism occupying a half space  $D_1$ ,  $z < 0$  with a metal film domain  $D_f$ ,  $d > z > 0$  of thickness  $d$  and a spherical penetrable particle with interior domain  $D_i$  and smooth boundary  $\partial D_i$  that is deposited above the film in the domain  $D_0$ ,  $z > d$  (Figure 11). Let the plane  $\Sigma_1$  separate a film and a glass prism and the plane  $\Sigma_f$  air and the film. Let us now introduce a Cartesian coordinate system  $Oxyz$  by choosing its origin  $O$  at the prism surface  $\Sigma_f$  such that the  $z$ -axis coincides with the axis of symmetry of the

particle and is directed into the domain  $D_0$ . We assume that the exciting field  $\{\mathbf{E}^0, \mathbf{H}^0\}$  is a linear polarized plane wave propagating inside the glass prism at angle  $\theta_1$  with respect to the  $z$ -axis. Placements of the objective lenses for two different setup schemes are marked in Figure 11 by letters A (for the conventional scheme) and B (for the alternative one).

The mathematical statement of the scattering problem is similar to Equation (1) but with different boundary conditions at the particle's surface:

$$\begin{aligned} \mathbf{n}_i \times (\mathbf{E}_i(p) - \mathbf{E}_0(p)) &= 0, \\ \mathbf{n}_i \times (\mathbf{H}_i(p) - \mathbf{H}_0(p)) &= 0, \end{aligned} \quad p \in \partial D_i. \quad (26)$$

The solution of the boundary value problem is constructed following the DSM scheme [38]. First of all, the diffraction problem of the plane wave  $\{\mathbf{E}^0, \mathbf{H}^0\}$  on the layered interface is solved. The resulting exciting field  $\{\mathbf{E}_\zeta^0, \mathbf{H}_\zeta^0\}$ ,  $\zeta = 0, f, 1$  satisfies the transmission conditions at  $\Sigma_1$  and  $\Sigma_f$ . Then we construct an approximate solution of the problem (26) for the scattered field  $\{\mathbf{E}_\zeta^S, \mathbf{H}_\zeta^S\}$  in domains  $D_\zeta$ ,  $\zeta = 0, f, 1$  and the total field inside particle  $D_i$ . Following the DSM scheme, the electromagnetic fields are represented as a finite linear combination of fields of dipoles and multipoles, which analytically satisfy the transmission conditions enforced at the plane interfaces  $\Sigma_1$  and  $\Sigma_f$  [7]. The approximate solution satisfies Maxwell equations in domains  $D_{0,1,f,i}$  the infinity conditions and the transmission conditions at the plane interfaces. Thus, the scattering problem is reduced to the problem of approximating of the exciting field on the particle surface  $\partial D_i$ . The amplitudes of the DS are determined from the boundary conditions at the particle surface, which can be rewritten as follows:

$$\begin{aligned} \mathbf{n}_i \times (\mathbf{E}_i(p) - \mathbf{E}_0(p)) &= \mathbf{n}_i \times \mathbf{E}_0^0(p), \\ \mathbf{n}_i \times (\mathbf{H}_i(p) - \mathbf{H}_0(p)) &= \mathbf{n}_i \times \mathbf{H}_0^0(p), \end{aligned} \quad p \in \partial D_i \quad (27)$$

where  $\{\mathbf{E}_0^0, \mathbf{H}_0^0\}$  is a plane wave refracted into the upper semi-space  $D_0$ .

To construct the fields of dipoles and multipoles that analytically satisfy the transmission conditions at the plane interfaces  $\Sigma_1$  and  $\Sigma_f$  we apply the Green's tensor for a stratified interface (Equation (4)). Associated spectral functions  $v_{11}^{e,h}, v_{33}^{e,h}, v_{31}^{e,h}$  providing transmission conditions enforced at  $z = 0, d$  accept the following forms

$$v_{11}^{e,h}(\lambda, z, z_0) = \begin{cases} \frac{\exp\{-\eta_0|z - z_0|\}}{\eta_0} + A_{11}^{e,h}(\lambda, z_0) \exp\{-\eta_0|z - d|\}, & z \geq d, z_0 > 0, \\ B_{11}^{e,h}(\lambda, z_0) \exp\{-\eta_f|z - d|\} + C_{11}^{e,h}(\lambda, z_0) \exp\{-\eta_f z\}, & d \geq z \geq 0 \\ D_{11}^{e,h}(\lambda, z_0) \exp\{\eta_1 z\}, & z \leq 0 \end{cases}$$

$$v_{33}^{e,h}(\lambda, z, z_0) = \begin{cases} \frac{\exp\{-\eta_0|z - z_0|\}}{\eta_0} + A_{33}^{e,h}(\lambda, z_0) \exp\{-\eta_0|z - d|\}, & z \geq d, z_0 > 0 \\ B_{33}^{e,h}(\lambda, z_0) \exp\{-\eta_f|z - d|\} + C_{33}^{e,h}(\lambda, z_0) \exp\{-\eta_f z\}, & d \geq z \geq 0 \\ D_{33}^{e,h}(\lambda, z_0, d) \exp\{-\eta_1 z\}, & z \leq 0 \end{cases}$$

$$v_{31}^{e,h}(\lambda, z, z_0) = \begin{cases} A_{31}^{e,h}(\lambda, z_0) \exp\{-\eta_0|z - d|\}, & z \geq d, z_0 > 0, \\ B_{31}^{e,h}(\lambda, z_0) \exp\{-\eta_f|z - d|\} + C_{31}^{e,h}(\lambda, z_0) \exp\{-\eta_f z\}, & d \geq z \geq 0 \\ D_{31}^{e,h}(\lambda, z_0) \exp\{\eta_1 z\}, & z \leq 0. \end{cases} \quad (28)$$

The corresponding coefficients  $A_{\alpha\beta}^{e,h}, B_{\alpha\beta}^{e,h}, C_{\alpha\beta}^{e,h}, D_{\alpha\beta}^{e,h}$  are determined from the conditions (8).

Following the scheme described in Section 2, we will construct an approximate solution that accounts both for the axial symmetry of the scattering problem and the polarization of the exciting field. Let us consider a  $P$ -polarized exciting plane wave first. In this case, the refracted plane wave in  $D_0$  has the following representation:

$$\begin{aligned} \mathbf{E}_0^0 &= T_{01}^P(-\mathbf{e}_x \cos \theta_0 + \mathbf{e}_z \sin \theta_0) \\ &\quad \times \exp\{-jk_0(x \sin \theta_0 + z \cos \theta_0)\}, \\ \mathbf{H}_0^0 &= -T_{01}^P n_0 \mathbf{e}_y \exp\{-jk_0(x \sin \theta_0 + z \cos \theta_0)\}, \end{aligned} \quad (29)$$

where  $(\mathbf{e}_x, \mathbf{e}_y, \mathbf{e}_z)$  is basis of the Cartesian coordinate system, and  $T_{01}^P$  is the transmission coefficient for  $P$ -polarization associated with the multi-layered interface

$$T_{01}^P = \frac{t_{1f}^P t_{f0}^P \exp(-jk_f \cos \theta_f d)}{1 + r_{1f}^P r_{f0}^P \exp(-2jk_f \cos \theta_f d)}.$$

Here,  $\theta_\zeta$  is the angle of refraction in  $D_\zeta$ ,  $\zeta = 0, f$ , and  $r_{\alpha\beta}^P, t_{\alpha\beta}^P$  are reflection and transmission coefficients introduced in Equation (3).

Now we consider  $S$ -polarized excitation. In this case, the field of the plane wave refracted in  $D_0$  is:

$$\begin{aligned} \mathbf{E}_0^0 &= T_{01}^S \mathbf{e}_y \exp\{-jk_0(x \sin \theta_0 + z \cos \theta_0)\}, \\ \mathbf{H}_0^0 &= T_{01}^S n_0 (-\mathbf{e}_y \cos \theta_0 + \mathbf{e}_z \sin \theta_0) \\ &\quad \times \exp\{-jk_0(x \sin \theta_0 + z \cos \theta_0)\}, \end{aligned} \quad (30)$$

where

$$T_{01}^S = \frac{t_{1f}^S t_{f0}^S \exp(-jk_f \cos \theta_f d)}{1 + r_{1f}^S r_{f0}^S \exp(-2jk_f \cos \theta_f d)}.$$

Corresponding to Snell's law:  $n_0 \sin \theta_0 = n_1 \sin \theta_1$ . When the incident angle exceeds the critical one  $\theta_1 > \theta_c = \arcsin(n_0/n_1)$ ,  $n_1 > n_0$  the exciting wave is totally reflected from the upper interface  $\Sigma_f$ . In this case, only an evanescent wave, which propagates along the plane surface  $\Sigma_f$  and decays along the  $z$  direction remains in the upper half-space  $D_0$ .

The approximate solution of the scattering problem based on the DSM fulfils the transmission conditions on plane interfaces  $\Sigma_1$  and  $\Sigma_f$ , and accounts for the rotational symmetry of the scattering problem geometry and polarization of the exciting field [7]. It accepts the form of Equations (14) and (18) with the obvious changes of the spectral functions (28). DS amplitudes are determined from the transmission conditions (27) enforced at the particle surface  $\partial D_i$ . By resolving the exciting field (Equations (29) and (30)) in Fourier series similar to Equation (10) we proceed from surface approximation to a set of 1D approximating problems on the surface meridian, as described in Section 1. The latter problems are solved by using a GPM approach as described above.

Once the Fourier harmonics of the DS amplitudes  $\{p_{nm}^f, q_{nm}^f, r_n^f\}$  are determined, one can compute the far field patterns  $\mathbf{F}_{0,1}(\theta, \varphi)$  (Equations (20) and (21)) in  $D_{0,1}$  domains. But in contrast with the previous section, spectral functions (22) corresponding to  $D_0$  domain have the form [38]

$$\begin{aligned} \bar{g}_{nm}^{e,h(0)} &= \exp\{jk_0 z_n \cos \theta\} + jk_0 \cos \theta \exp\{jk_0 d \cos \theta\} \\ &\quad \times A_{11}^{e,h}(k_0 \sin \theta, w_n, d) \\ \bar{f}_{nm}^{e,h(0)} &= jk_0 \cos \theta \exp\{jk_0 d \cos \theta\} A_{31}^{e,h}(k_0 \sin \theta, w_n, d) \end{aligned}$$

where  $w_n$  are the complex coordinates of the DS associated with the scattered field.

Once the unknown amplitudes of DS are determined, the far field patterns for  $P$ - and  $S$ -polarization are represented as finite linear combinations of elementary functions (see Equations (20) and (21)). This circumstance ensures fast and effective computer analysis of the scattering characteristics in the far zone.

### 3.2. Numerical results and discussion

In this section we present computer simulation for two alternative schemes of TIRM. We consider following light scattering characteristics: the differential scattering cross-section (DSC), which is given by Equation (23) with the dimension of  $\mu\text{m}^2$ .

We will also consider an objective response as a function of height of the particle. It represents the integrated intensity scattered into the prescribed solid

angle  $\Omega$ , which corresponds to the numerical aperture of the objective lens:

$$\sigma_{0,1}^{P,S}(\theta_1) = \int_{\Omega} DSC_{0,1}^{P,S}(\theta_1, \theta, \varphi) d\omega. \quad (31)$$

The integral response is used to evaluate the scattered intensity captured by an objective lens [55].

We will consider a  $P$ - or  $S$ -polarized plane wave with a wavelength of  $\lambda = 633$  nm. The prism is made of glass with refractive index of  $n_1 = 1.52$  for this wavelength. The particles we consider are made of  $\text{SiO}_2$  with a refractive index  $n_i = 1.46$  and have diameters of  $D = 300$  nm, 600 nm and 1.2  $\mu\text{m}$ . The particles are situated in water with  $n_0 = 1.33$  on a gold film with  $n_f = 0.18 - 3.26j$  and thickness of  $d = 50$  nm. The critical angle for this system, where evanescent waves appear, is  $61.04^\circ$ . The incident angle is  $66.75^\circ$ . Scattered fields are captured by objectives with collecting angles of  $32^\circ$ . For technical reasons, the collector situated beneath the prism has a central hole of  $5^\circ$  to avoid detection of the specular beam. To reduce the intensity of the reflected plane wave we adjusted the film thickness and incident angle to reach the surface plasmon resonance regime.

In the following figures, the results of computational experiments are presented. In Figure 12 the objective response  $\sigma_{0,1}^{P,S}$  versus particle–film distance  $h$  is presented for particles of different diameters and both polarization of the incident light. The capturing objective is situated above the prism. We can see that all the curves have pronounced oscillating behavior. For some of them (e.g. for particle of  $D = 1.2 \mu\text{m}$ ) the fluctuation of the values is so extreme, that it is possible to choose three values of height where the value of  $\sigma_0^P$  seems to be the same. Such behavior of the objective response complicates the problem of determination of the particle height from the measured data.

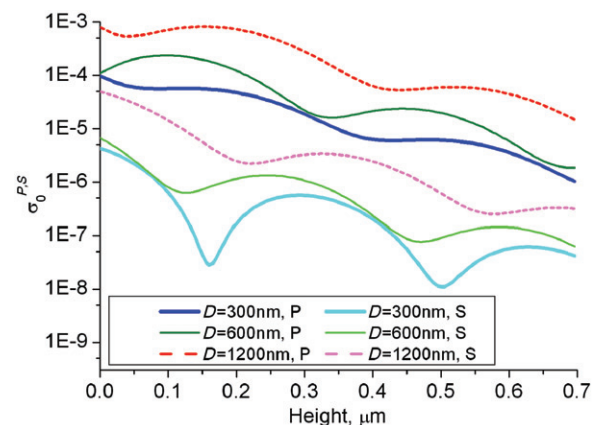


Figure 12. Particles of different diameters,  $P$  and  $S$ -polarizations, intensity above the prism. (The color version of this figure is included in the online version of the journal.)

To compare to these results we present similar computations for the case when the collecting objective is positioned beneath the prism (Figure 13). Now we observe a completely different behavior: all curves demonstrate monotonic almost exponential decay. In Figure 14 the results are presented for the particle of  $D = 300$  nm for positions of the collector both above and beneath the prism for  $P$ -polarized excitation. These results demonstrate that the intensity of  $P$ -polarized light is several orders higher than for the  $S$ -polarized one. Similar to the results presented above, both curves for the upper collector show oscillations, while both curves for the collector's deposition beneath the prism have monotonic exponential decay. Similar results for larger particles of  $D = 600$  nm

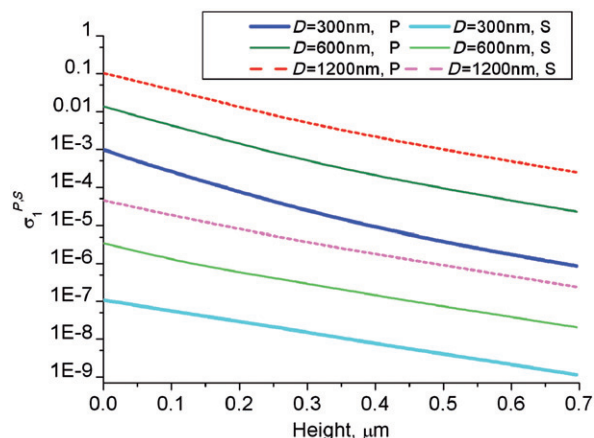


Figure 13. Particles of different diameters,  $P$ - and  $S$ -polarizations, intensity beneath the prism. (The color version of this figure is included in the online version of the journal.)

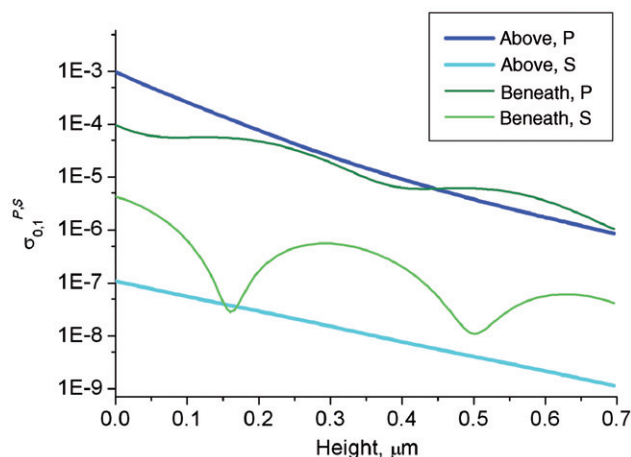


Figure 14. Particle of  $D = 300$  nm,  $P$ - and  $S$ -polarizations, different heights. (The color version of this figure is included in the online version of the journal.)

(Figure 15) and  $D = 1.2 \mu\text{m}$  (Figure 16) are presented as well.

Now we turn to analyze the behavior of the DSC in the incidence plane. Let us look at two particle heights where  $\sigma_0^P$  reaches almost the same values. The results for DSC distribution for the particle of  $D = 300$  nm are depicted in Figure 17. Here the range of observation angles  $90^\circ < \theta < 270^\circ$  belongs to the upper semi-plane and the range of  $270^\circ < \theta < 360^\circ$  belongs to the lower semi-plane. From the results presented above, one can see that in spite of the upper semi-plane the intensity values are nearly the same; at the lower semi-plane both values differ essentially. Additionally, it is clear that the maximum of intensity is directed towards the specular direction at  $\theta \approx 110^\circ$ . From comparison it is

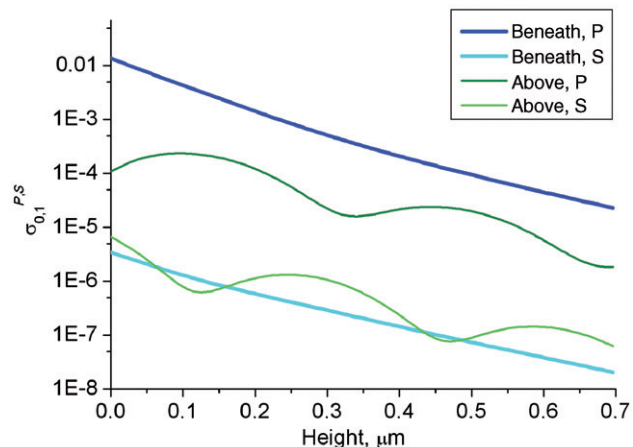


Figure 15. Particle of  $D = 600$  nm,  $P$ - and  $S$ -polarizations, different heights. (The color version of this figure is included in the online version of the journal.)

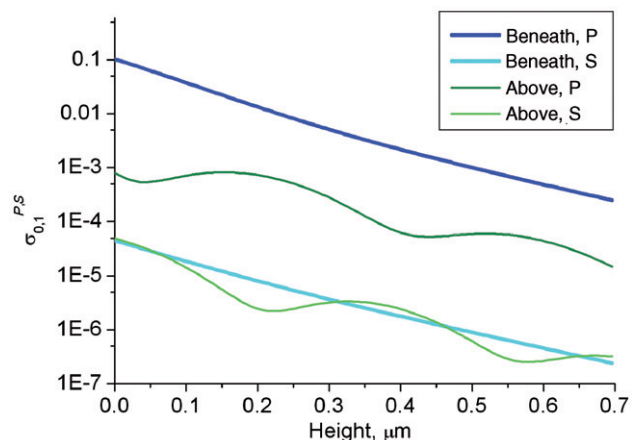


Figure 16. Particle of  $D = 1200$  nm,  $P$ - and  $S$ -polarizations, different heights. (The color version of this figure is included in the online version of the journal.)

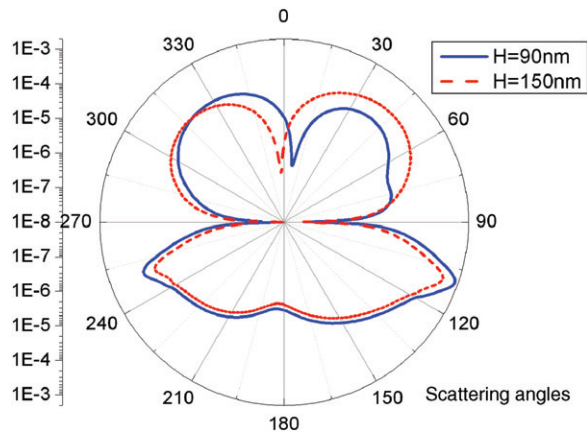


Figure 17. Particle  $D=300$  nm,  $P$ -polarization, different particle heights. (The color version of this figure is included in the online version of the journal.)

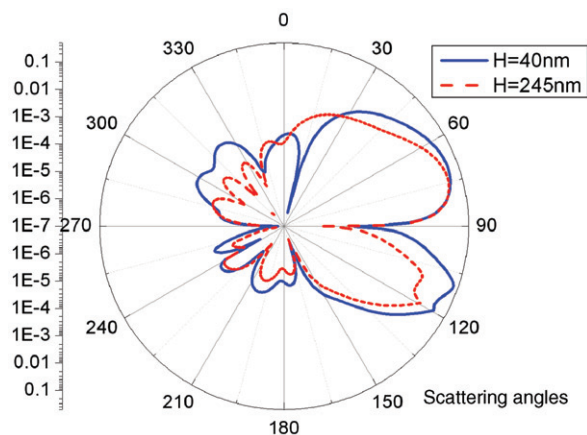


Figure 18. Particle  $D=1200$  nm,  $P$ -polarization, different particle heights. (The color version of this figure is included in the online version of the journal.)

also obvious that the difference of the intensity scattered to the upper semi-plane is much lower than the intensity at  $\theta \approx 110^\circ$ , despite the central  $5^\circ$  of the objective lens being cut to omit the influence of the specular beam.

Similar results are presented for the particle of  $D=1.2 \mu\text{m}$  (Figure 18). The results support the conclusions we made for the particle of smaller diameter. Due to these circumstances, the determination of the particle–film distance from observations of the intensity beneath the prism should be much easier, in contrast to the conventional observations in the upper domain.

#### 4. Conclusions

In this paper we presented a DSM-based model of two different measuring schemes of a TIRM setup. Computer simulation results of light scattered by a

particle above the filmed prism are presented. The results have demonstrated that the  $P$ -polarized response exceeds the  $S$ -polarized by several orders and that the TIRM scheme with the collector placed beneath the prism provides considerable advantages compared with the conventional scheme. In addition, computer simulation results show that the intensity scattered into the lower semi-space is higher than the intensity scattered into the upper semi-space. Additionally, the behavior of the  $\sigma_1^P$  curve beneath the prism demonstrates monotonic exponential decay that enables easier determination of the particle–film distance. Based on these analysis, we conclude that the alternative TIRM scheme is advantageous compared with the conventional one.

#### Acknowledgements

The authors gratefully acknowledge funding of this research by the Deutsche Forschungsgemeinschaft (DFG) and the Russian Foundation for Basic Research (RFBR).

#### References

- [1] Taflove, A.; Hagness, S. *Computational Electrodynamics: The Finite-difference Time-domain Method*; Artech House: Norwood, 2005.
- [2] Jin, J. *The Finite Element Method in Electromagnetics*; Wiley: Chichester, 1993.
- [3] Chaumet, P.C.; Rahmani, A.; Bryant, G.W. *Phys. Rev. B* **2003**, *67*, 165404.
- [4] Søndergaard, T. *Phys. Stat. Sol. B* **2007**, *244*, 3448–3462.
- [5] Hafner, C. *The Generalized Multiple Multipole Technique for Computational Electromagnetics*; Artech: Boston, MA, 1990.
- [6] Doicu, A.; Eremin, Yu.A.; Wriedt, T. *Acoustic and Electromagnetic Scattering Analysis Using Discrete Sources*; Academic Press: New York, 2000.
- [7] Eremin, Yu.A. *J. Commun. Techn. Electron.* **2000**, *45*, Suppl. 2, S269–S280.
- [8] Hafner, Ch. *Phys. Stat. Sol. B* **2007**, *244*, 3435–3447.
- [9] Capoglu, I.R.; Smith, G.S. *IEEE Trans. Antennas Propag.* **2006**, *52*, 3805–3814.
- [10] Alegret, J.; Johansson, P.; Käll, M. *New J. Phys.* **2008**, *10*, 105004.
- [11] Colton, D.; Kress, R. *Integral Equation Methods in Scattering Theory*; Wiley: New York, 1983.
- [12] Bharadwaj, P.; Deutsch, B.; Lukas Novotny, L. *Adv. Opt. Photon.* **2009**, *1*, 438–483.
- [13] Joannopoulos, J.D.; Johnson, S.G.; Winn, J.N.; Meade, R.D. *Photonic Crystals: Molding the Flow of Light*; Princeton University Press: Princeton, NJ, 2008.
- [14] Abdulhalim, M.Z.; Lakhtakia, A. *Electromagnetics* **2008**, *28*, 214–242.
- [15] Evlyukhin, B.; Brucoli, G.; Martín-Moreno, L.; Bozhevolnyi, S.; García-Vidal, F.J. *Phys. Rev. B* **2007**, *76*, 075426.

- [16] Simsek, E. *Opt. Express* **2010**, *18*, 1722–1733.
- [17] Jung, J.; Søndergaard, T. *Phys. Rev. B* **2008**, *77*, 245310.
- [18] Bobbert, P.A.; Vlieger, J. *Physica* **1986**, *137A*, 209–242.
- [19] Eremin, Yu.; Orlov, N. *Appl. Opt.* **1996**, *35*, 6599–6604.
- [20] Novotny, L.; Hecht, B.; Pohl, D. *J. Appl. Phys.* **1997**, *81*, 1798–1806.
- [21] Schmehl, R.; Nebeker, B.M.; Hirleman, E.D. *J. Opt. Soc. Am. A* **1997**, *14*, 3026–3036.
- [22] Eremin, Yu.A.; Ivakhnenko, V.I. *Moscow University Comput. Math. Cybernetics*. **1998**, *2*, 15–23.
- [23] Doicu, A.; Eremin, Yu.A.; Wriedt, T. *Opt. Commun.* **1999**, *159*, 266–277.
- [24] Sung, L.; Mulholland, G.W.; Germer, T.A. *Opt. Lett.* **1999**, *24*, 866–868.
- [25] Videen, G. *J. Opt. Soc. Am. A* **1001**, *8*, 483–489.
- [26] Taubenblatt, M.A.; Tran, T.K. *J. Opt. Soc. Am. A* **1993**, *10*, 912–919.
- [27] Ebbesen, T.W.; Lezec, H.J.; Ghaemi, H.F.; Thio, T.; Wolff, P.A. *Nature* **1998**, *391*, 667–669.
- [28] Wannemacher, R. *Opt. Commun.* **2001**, *195*, 107–118.
- [29] Genet, C.; Ebbesen, T.W. *Nature* **2007**, *445*, 39–46.
- [30] de Abajo, F.J.G. *Rev. Mod. Phys.* **2007**, *79*, 1267–1290.
- [31] Shuford, K.L.; Gray, S.K.; Ratner, M.A.; Schatz, G.C. *Chem. Phys. Lett.* **2007**, *435*, 123–126.
- [32] Laluet, J.-Y.; Drezet, A.; Genet, C.; Ebbesen, T.W. *New J. Phys.* **2008**, *10*, 105014.
- [33] Przybilla, F.; Degiron, A.; Genet, C.; Ebbesen, T.W.; de León-Pérez, F.; Bravo-Abad, J.; García-Vidal, F.J.; Martín-Moreno, L. *Opt. Express* **2008**, *16*, 9571–9579.
- [34] de Dood, M.J.; Driessen, E.F.C.; Stolwijk, D.; van Exter, M.P. *Phys. Rev. B* **2008**, *77*, 115437.
- [35] Park, T.H.; Mirin, N.; Lassiter, J.B.; Nehl, C.L.; Halas, N.J.; Nordlander, P. *ACS Nano*. **2008**, *2*, 25–32.
- [36] Alaverdyan, Y.; Sepulveda, B.; Eurenus, L.; Olsson, E.; Kall, M. *Nature Phys.* **2007**, *3*, 884–889.
- [37] Gordon, R.; Sinton, D.; Kavanagh, K.L.; Brolo, A.G. *Acc. Chem. Res.* **2008**, *41*, 1049–1057.
- [38] Eremin, Yu.A.; Sveshnikov, A.G. *Comput. Maths. Math. Phys.* **2007**, *47*, 262–279.
- [39] Eremina, E.; Eremin, Y.; Grishina, N.; Wriedt, T. *Opt. Commun.* **2008**, *281*, 3581–3586.
- [40] Eremina, E.; Eremin, Y.; Grishina, N.; Wriedt, T. *J. Comput. Theor. Nanosci.* **2009**, *6*, 786–803.
- [41] Grishina, N.; Eremin, Yu.A.; Sveshnikov, A.G. *Opt. Spectrosc.* **2009**, *106*, 753–756.
- [42] Maier, S. *Plasmonics: Fundamentals and Applications*; Springer: New York, 2007.
- [43] Chew, W.C. *Waves and Fields in Inhomogeneous Media*; IEEE Press: Piscataway, NJ, 1995.
- [44] Eremin, Yu.A. *Sov. Phys. Dokl.* **1983**, *28*, 451–452.
- [45] Eremin, Yu.A.; Orlov, N.V.; Sveshnikov, A.G. Models of Electromagnetic Scattering Problems Based on Discrete Sources Methods. In *Generalized Multipole Techniques for Electromagnetic and Light Scattering*; Wriedt, T., Ed.; Elsevier Science: Amsterdam, 1999; pp 39–79.
- [46] Walz, J. *Curr. Opin. Colloid. Interface Sci.* **1997**, *2*, 600–606.
- [47] Prieve, D.C. *Adv. Colloid. Interface Sci.* **1999**, *82*, 93–125.
- [48] Berg-Sørensen, K.; Flyvbjerg, H. *Rev. Sci. Instrum.* **2004**, *75*, 594–612.
- [49] Volpe, G.; Volpe, G.; Petrov, D. *Phys. Rev. E* **2007**, *76*, 061118.
- [50] Bevan, M.A.; Prieve, D.C. *Langmuir* **1999**, *15*, 7925–7936.
- [51] Hertlein, C.; Helden, L.; Gambassi, A.; Dietrich, S.; Bechinger, C. *Nature* **2008**, *451*, 172–175.
- [52] Blickle, V.; Babic, D.; Bechinger, C. *Appl. Phys. Lett.* **2005**, *87*, 101102.
- [53] Piech, M.; Weronki, P.; Wu, X.; Walz, J.Y. *J. Colloid Interface Sci.* **2002**, *247*, 327–341.
- [54] Helden, L.; Roth, R.; Koenderink, G.H.; Leiderer, P.; Bechinger, C. *Phys. Rev. Lett.* **2003**, *90*, 048301.
- [55] von Grunberg, H.H.; Helden, L.; Leiderer, P.; Bechinger, C. *J. Chem. Phys.* **2001**, *114*, 10094–10104.
- [56] Helden, L.; Eremina, E.; Eremin, Y.; Riefler, N.; Hertlein, C.; Bechinger, C.; Wriedt, T. *Appl. Opt.* **2006**, *45*, 7299–7308.
- [57] Eremin, Y.; Wriedt, T. *J. Quant. Spectrosc. Radiat. Transfer* **2004**, *89*, 53–65.
- [58] Hertlein, C.; Riefler, N.; Eremina, E.; Wriedt, T.; Eremin, Y.; Helden, L.; Bechinger, C. *Langmuir* **2008**, *24*, 1–4.